Radiative properties of aerosol mixture observed during the dry season 2006 over M'Bour, Senegal (African Monsoon Multidisciplinary Analysis campaign)

Y. Derimian,[1] J.-F. Léon,[1] O. Dubovik,[1] I. Chiapello,[1] D. Tanré,[1] A. Sinyuk,[2,3] F. Auriol,[1] T. Podvin,[1] G. Brogniez,[1] and B. N. Holben[2]

Received 1 February 2008; revised 22 April 2008; accepted 13 June 2008; published 6 September 2008.

[1] During the dry season in the Western Africa region the outbreaks of biomass burning aerosols occur on a background of frequent dust storms. In the frame of the African Monsoon Multidisciplinary Analysis (AMMA) campaign we studied optical properties and radiative effects of aerosol mixture and dust observed from January to March 2006 over M'Bour, Senegal. The aerosol burden during the observing period was notably below the average of previous years. However, variability of aerosol sizes and spectral absorption were found as representative. The lidar obtained extinction profiles suggested aerosol transport in two layers (or one elevated layer) for events with two different aerosol types, called aerosol mixture in the paper. Low-altitude transport was observed for dust. The broadband solar radiative fluxes and aerosol radiative effects were analyzed by combining measurements and simulations. The simulations relied on retrieved column aerosol properties and are products of Aerosol Robotic Network data processing. The 24-h average aerosol radiative effect yielded cooling at the bottom and at the top of the atmosphere for all the analyzed events of aerosol mixture and dust. The radiative efficiency (radiative effect scaled by optical thickness) at the bottom of the atmosphere and within the aerosol layer appeared to be stronger in case of mixture than in case of pure dust due to enhanced absorption ability of former. We also evaluated the importance of accounting for dust particles nonsphericity for simulating radiative effects. Our test showed that neglecting of aerosol particle shape can result in pronounced bias, up to 10% overestimation of daily average aerosol radiative effect.

Citation: Derimian, Y., J.-F. Léon, O. Dubovik, I. Chiapello, D. Tanré, A. Sinyuk, F. Auriol, T. Podvin, G. Brogniez, and B. N. Holben (2008), Radiative properties of aerosol mixture observed during the dry season 2006 over M'Bour, Senegal (African Monsoon Multidisciplinary Analysis campaign), *J. Geophys. Res.*, *113*, D00C09, doi:10.1029/2008JD009904.

1. Introduction

[2] The Western Africa region appears to be strongly affected by significant concentrations of biomass burning aerosols and airborne mineral dust during the dry season. This is a quite unique area where the mixture of biomass burning and dust occurs and is expected to have significant impact on radiative balance of the solar radiation. Often aerosol particles over the Western Africa region are characterized by long-range transport. Thus, the mixture of biomass burning and dust aerosols may have significant radiative and climatic impacts not only on the regional but also on the global scale. However, optical properties of such an aerosol mixture and its effect on solar radiation are poorly documented. Previous field campaigns in Africa were devoted to the characterization of either dust or biomass burning aerosols but not to their mixture. Mineral dust outbreaks in Western Africa were studied during Saharan Dust Experiment (SHADE) [*Tanré et al.*, 2003], where dust radiative effect was assessed in solar and terrestrial spectrum based on measurements [*Haywood et al.*, 2003; *Highwood et al.*, 2003] and model calculations [*Myhre et al.*, 2003]. The aerosol particles in this experiment were found as representative of Saharan dust without biomass burning contamination [*Formenti et al.*, 2003] and had relatively low absorbing properties [*Haywood et al.*, 2003]. The other intensive field campaigns SAFARI-92 and SAFARI-2000 were conducted in the southern Africa region [*Swap et al.*, 2002; *Eck et al.*, 2003; *Ichoku et al.*, 2003; *Privette and Roy*, 2005], an area which is not effectively influenced by dust and observations were mostly addressed to smoke emission by fires. The mixture of urban or industrial pollution with dust frequently occurs in the Mediterranean basin and Asia [e.g., *Ramanathan et al.*, 2001]. However, radiative effect of dust and biomass burning mixture can be different from the

[1]Laboratoire d'Optique Atmosphérique, Université des Sciences et Technologies de Lille, CNRS, Villeneuve d'Ascq, France.
[2]Laboratory for Terrestrial Physics, NASA Goddard Space Flight Center, Greenbelt, Maryland, USA.
[3]Science Systems and Applications, Inc., Lanham, Maryland, USA.

Copyright 2008 by the American Geophysical Union.
0148-0227/08/2008JD009904

mixture with urban or industrial aerosols due to different spectral absorption properties of biomass burning aerosol compared to urban or industrial pollution [*Kirchstetter et al.*, 2004; *Andreae and Gelencser*, 2006].

[3] This investigation is part of the comprehensive observation period during the African Monsoon Multidisciplinary Analysis (AMMA) campaign in West Africa. It includes ground-based remote sensing measurements by the instruments located in M'Bour, Senegal. This site is predominantly influenced by dust during the whole year, [e.g., *Chiapello et al.*, 1997; *Kaufman et al.*, 2005], but outbreaks of biomass burning aerosols occur in wintertime [e.g., *Holben et al.*, 2001]. Several episodes of aerosol mixture occurred from January to February 2006 during the special observing period (SOP-0) of AMMA, followed by episodes of airborne dust intrusions in March 2006. The selected episodes are also presented in context of data from 10 years of observations of key aerosol parameters at the long-term AERONET/PHOTONS site in M'Bour. The aerosol mixture and dust events are analyzed in terms of aerosol optical properties, vertical profiles, downward flux measurements, and calculated radiative effect. The measured broadband radiative flux is compared to the flux calculated by an atmospheric radiative transfer forward model as used in AERONET retrieval code. In addition, the effects of particle nonsphericity in radiative forcing simulations are often neglected and this approximation is presently checked thanks to either aerosol spherical or nonspherical models available in the AERONET code calculations.

[4] In summary, the study had the following objectives: (1) characterization of biomass burning aerosol mixture with dust and comparison with pure dust events in the Western Africa region; (2) representativeness of aerosol parameters observed during the intensive period of measurements; (3) analysis of the measured downward radiative flux at the surface and comparison with the calculated flux; (4) assessment of calculated aerosol radiative effect and efficiency for observed mixed aerosols and comparison with those of pure dust; (5) quantitative evaluation of accounting for particles nonsphericity in the estimation of radiative effects due to the presence of pure dust and aerosol mixture.

2. Site Description

[5] The M'Bour site (14°23′38″N, 16°57′32″W) is located in Senegal, 80 km south of Dakar. The instruments are placed on the roof of the Institut de Recherche et Développement (IRD) building, which is located at proximity of the seashore, on the Atlantic coast, south of the city of M'Bour. The climatic conditions in Senegal are characterized by a dry season from roughly November to May and a rainy season from June to October, with the monsoon onset and the return to the dry season changing from year to year. The dominant winds in Senegal are the north to northeast maritime trade winds, the Harmattan, which has a dominant east direction, and the monsoon (in summer). The M'Bour site is located on the path of most Saharan dust outbreaks transported westward over the northern tropical Atlantic and is also under the influence of biomass burning events that occur during the dry season (mostly from December to March). It is thus well suitable for studying the properties of the mixture of these two aerosol components.

3. Instrumentation and Data Sets

[6] The measurements used in this study were obtained from (1) a CIMEL sun/sky photometer, part of the AERONET/PHOTONS program; (2) Kipp and Zonen CM22 pyranometer; (3) Kipp and Zonen CH1 pyrheliometer; and (4) a CIMEL micropulse backscattering LIDAR system. All the instruments were collocated on the roof of a 12 m height building (see Figure 1).

3.1. Sun/Sky Photometer

[7] In this study we use the data obtained from the CIMEL instrument located in M'Bour (also named as Dakar site) and operated by PHOTONS, which is the French part of AERONET [*Holben et al.*, 1998]. The CIMEL spectral polar photometer performs direct sun measurements every 15 min, with a 1.2° field of view at the 440, 675, 870, 940, and 1020 nm nominal wavelengths. The 940 nm channel is used to retrieve water vapor content. The angular distribution of sky radiance is also measured at 440, 670, 870, and 1020 nm. These sky radiances together with AOT measured at the same wavelengths are used to derive detailed aerosol optical properties including aerosol size distribution, absorption, refractive index, etc., as described by *Dubovik and King* [2000]. The retrieval scheme was recently updated with several improvements. For example, the new retrieval considers mixture of polydisperse, randomly oriented, homogeneous spheroids with a fixed distribution of aspect ratios [*Mishchenko et al.*, 1997]. Accordingly, the new retrieval includes fraction (in percentage) of spherical particles as a new parameter (see details in the work of *Dubovik et al.* [2006]). This distribution provides the best fit [*Dubovik et al.*, 2006] to detailed laboratory measurements of polarimetric properties of light scattered by in situ dust sample [*Volten et al.*, 2001]. Another important update is that the new retrievals use surface reflectance derived from satellite observation climatology. It results in notable improvements in the retrieval of the refractive index and single-scattering albedo in some specific observation conditions [*Sinyuk et al.*, 2007].

[8] This new retrieval (using spheroid model) of aerosol properties (O. Dubovik et al., manuscript in preparation, 2008) is currently available on the AERONET Web site and labeled as "Version 2 (V2) inversion products." The present study uses Version 2 aerosol retrieval products. The data analysis is performed for cloud-free conditions (as prescribed by *Smirnov et al.* [2000] algorithm) and all the restrictions recommended by *Dubovik et al.* [2002] for reliability of the inversion product are applied.

3.2. Pyranometer and Normal Incidence Pyrheliometer

[9] The downward broadband shortwave radiative flux is measured in the spectral range from 200 to 3600 nm using the Kipp and Zonen CM22 pyranometer with a time step of 2 min. In order to measure the diffuse radiation, the direct solar radiation is intercepted by a 60 mm diameter sphere shadower tracking the Sun. The CM22's field of view is 2π sr; however, the measurement error depends on the solar zenith angle and generally increases with the solar zenith

Figure 1. The instrumentation setup at the M'Bour site in Senegal: (1) a CIMEL sun/sky photometer, part of the AERONET/PHOTONS program; (2) Kipp and Zonen CM22 pyranometer; (3) Kipp and Zonen CH1 pyrheliometer; and (4) a CIMEL micropulse backscattering LIDAR system.

angle. The pyranometer sensitivity on the temperature is corrected for. The solar direct radiative flux, in the spectral range from 200 to 4000 nm, is measured by the Kipp and Zonen CH1 pyrheliometer in a full angle of 5° ± 0.2°. The sensitivity also depends on the instrument temperature. The total radiative flux at the surface is then calculated as the sum of the measured diffuse and direct fluxes. The total flux can be compared to the pyranometer measurements when the shadower is removed. This procedure was conducted in the beginning of the measurement period (February 2006) and one year afterward (February 2007), as part of the calibration test. The relative error between the total flux measured by the pyranometer and the one resulting from the sum of the diffuse and direct flux was −0.5% in February 2006 and +1.0% in February 2007. The proper shadowing of the pyranometer and the differences in the upper spectral range of the pyranometer and the pyrheliometer, 3600 and 4000 nm, respectively, can partly explained the discrepancy. The underestimation of the total flux, measured by the pyranometer, due to the different spectral range, is around 0.3%. Moreover, the instruments sensitivity changes with time and with exposure to radiation. Both instruments were new at the beginning of the experiment and reported variation in the instrumental sensitivity is given as 0.5% per year for pyranometer and less than 1% per year for pyrheliometer. The manufacturer recommends calibration every 2 years when our data are acquired over 11 months only, from January to November 2006.

[10] The uncertainty in the flux measurements was estimated based on the variation in instrumental sensitivity per year, directional error, the temperature dependence, and deviation in sensitivity over irradiance range. The uncertainties were estimated as less than 1.6% for the diffuse flux at the SZA < 70° and less than 2.6% for the diffuse flux at the SZA of about 75°, for any azimuth direction. The instrumental uncertainty for the direct flux measurements was estimated as less than 1.5%. The uncertainty in the total flux measurements was estimated as less than about 2% and 3%, respectively, for SZA < 70° and at about 75°, and for any azimuth direction.

3.3. LIDAR

[11] The lidar system has been set up in January 2006 at M'Bour, few meters from the Sun photometer. The system is a 532 nm micropulse backscattering LIDAR manufactured by CIMEL. It is an eye-safe system emitting 4 μJ pulse of light with a frequency of 4.7 kHz. The vertical resolution is 15 m. The range of observation is between 210 m up to ~15 km in clear conditions. The LIDAR is operating for a period of 10 min every 20 min and we store 10 profiles averaged over 1 min. It has been working continuously from January to November 2006. The sky background noise is estimated by an average signal from the far field above 22 km, where the laser contribution is negligible. The LIDAR profiles are range corrected and the raw LIDAR profiles are then normalized to the molecular backscattering in the free troposphere using the molecular density vertical profile from the standard atmosphere. The aerosol extinction coefficient is retrieved from the attenuated LIDAR backscattering coefficient following [*Klett*, 1981] method. The atmospheric aerosol optical thickness is estimated using Sun photometer AOT interpolated at 532 nm from the measurements at 440 and 675 nm for exact coincidence with the LIDAR observations. The aerosol optical thickness is used to constrain the LIDAR extinction profile retrieval. In this study we present the daily mean aerosol extinction profiles. The aerosol optical thickness during the selected days is stable so the daily mean profile is expected to be representative.

4. Observations and Data Analysis

4.1. M'Bour: Special Observing Period Versus Long-Term Observations

[12] Special observing period (SOP) conducted during January–February 2006 (SOP-0) of the AMMA project was dedicated to characterization of the dry phase of the monsoon cycle. During the dry season biomass burning aerosols originate from the anthropogenic activities [*Liousse et al.*, 1996] and may interact with mineral dust in the region of interest. The presented work focused on characterization of airborne aerosol properties and its radiative effect during January–February 2006 when the probability of biomass burning aerosols mixture with mineral dust was high. The biomass burning aerosol supply was significantly reduced after the dry season while dust episodes continued to govern over the region. In order to trace this change in the aerosol impact we analyzed aerosol events from the followed month, March 2006. We first analyzed climatology of aerosol optical thickness of extinction (AOT or τ_{ext}), single scattering albedo (SSA or ω_0), and Ångström exponent (α). The single-scattering albedo is the ratio of light scattering to total light extinction (scattering and absorption) and represents scattering effectiveness relative to total extinction. Therefore, SSA decreases when absorption increases. We also used the difference between SSA at 440 nm and 1020 nm (DSSA or $\Delta\omega_0$), which characterizes the SSA spectral behavior. The negative values of $\Delta\omega_0$ can be related

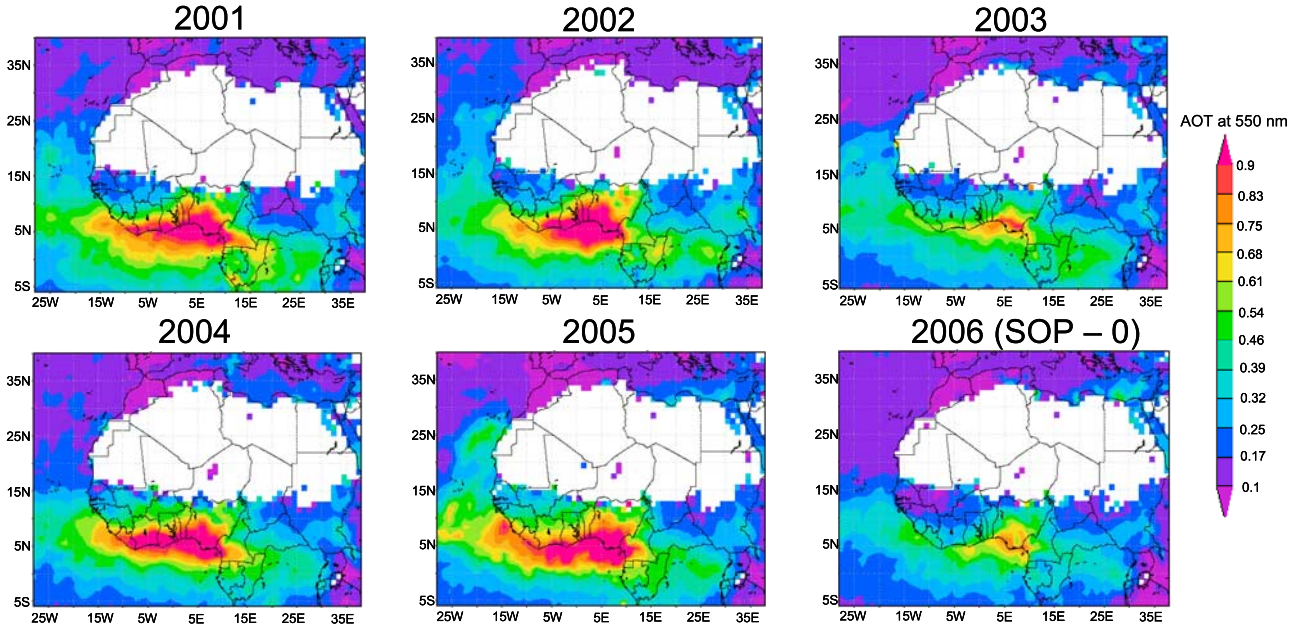

Figure 2. Mean values of aerosol optical thickness at 550 nm derived from the MODIS space instrument for the period of January–February for 6 years starting from 2001. The data for 2006 represents spatial pattern of aerosol loading during the special observing period (SOP-0) of the AMMA campaign. The plots are constructed from MODIS Terra Daily Collection 5 by the Giovanni MODIS Online Visualization and Analysis System (MOVAS) http://lake.nascom.nasa.gov/movas/.

to dust, where lower ω_0 at 440 nm is due to absorption by iron oxides, e.g., [*Sokolik and Toon*, 1999]. The positive values of $\Delta\omega_0$ can be attributed to urban, industrial or biomass burning aerosols [*Dubovik et al.*, 2002], which include strongly absorbing carbonaceous particles. The Ångström exponent describes the spectral dependence of aerosol optical thickness and is sensitive to variability of aerosol sizes. Thus, τ_{ext}, ω_0, $\Delta\omega_0$, and α in our analysis represent information on aerosol loading, spectral absorption properties, and the aerosol size.

[13] We first check if the aerosol characteristics observed during SOP-0 are representative of standard conditions observed over the previous years. The general pattern of atmospheric aerosol loading over the West Africa region is analyzed using MODIS derived AOT at 550 nm [*Kaufman et al.*, 1997; *Tanré et al.*, 1997; *Remer et al.*, 2005]. The mean values of AOT during the period of January–February for the years from 2001 to 2006 are presented in Figure 2. It can be noted that in 2006 (SOP-0) the aerosol loading was clearly lower than in the other years (except in 2003), especially for the regions known as affected by biomass burning aerosols. These low aerosol concentrations are worth of attention in the sense of representativeness of the assessed aerosol radiative effect during SOP-0 of AMMA 2006. It also may have an impact on studies of other climatic processes related to the aerosol concentrations and transport.

[14] In addition to the satellite data on a large spatial scale we check the representativeness of AERONET/PHOTONS ground-based measurements at the M'Bour site. Figures 3a, 3c, and 3d show τ_{ext}, $\Delta\omega_0$(440–1020), ω_0 at 1020 nm, and α during January, February, and March 2006 along with the all observations conducted from 1996 to 2006 at M'Bour. Figure 3b shows the mean values and standard deviations of τ_{ext} versus α for the periods of (1) January–February 2006 (SOP-0); (2) January–February from 1996 to 2006; and (3) all the observations from 1996 to 2006. It should be noted that January–February period for the years 1996–2006 includes only 7 years of data due to some gaps in the acquisition. The data analysis reveals that aerosol loading (mean τ_{ext}) during SOP-0 was 25% lower than the mean value for the same period of the previous years and 40% lower than the mean value for all the observations at the M'Bour site. The mean value of Ångström exponent was higher than the mean for the same period of the previous years and for all the observations. It suggests that during SOP-0 aerosol loading was lower with particles smaller than the average. Therefore SOP-0 appears to be less influenced by airborne mineral dust with lower concentration of biomass burning aerosol. At the same time, the range of the standard deviations of α had a good coverage of the possible values (Figures 3a and 3b), which indicates wide diversity of the aerosol sizes represented during SOP-0.

[15] Spectral features of single scattering albedo for elevated aerosol loadings (τ_{ext} at 440 nm > 0.4) were analyzed for different aerosol size classes. For example, Figure 3c reveals high negative $\Delta\omega_0$ for increased contribution of coarse particles ($0 < \alpha < 0.4$) in March, which characterized the mineral dust short-wavelength absorption by iron oxides. However, the $\Delta\omega_0$ during January and February was increasing and becoming positive for higher α, which indicates the presence of small size particles with enhanced absorption at the long-wavelength. In addition to the relative values of the difference ($\Delta\omega_0$), the absolute values of $1-\omega_0$ at 1020 nm (Figure 3d) suggests generally low absorption at 1020 nm by coarse particles in March

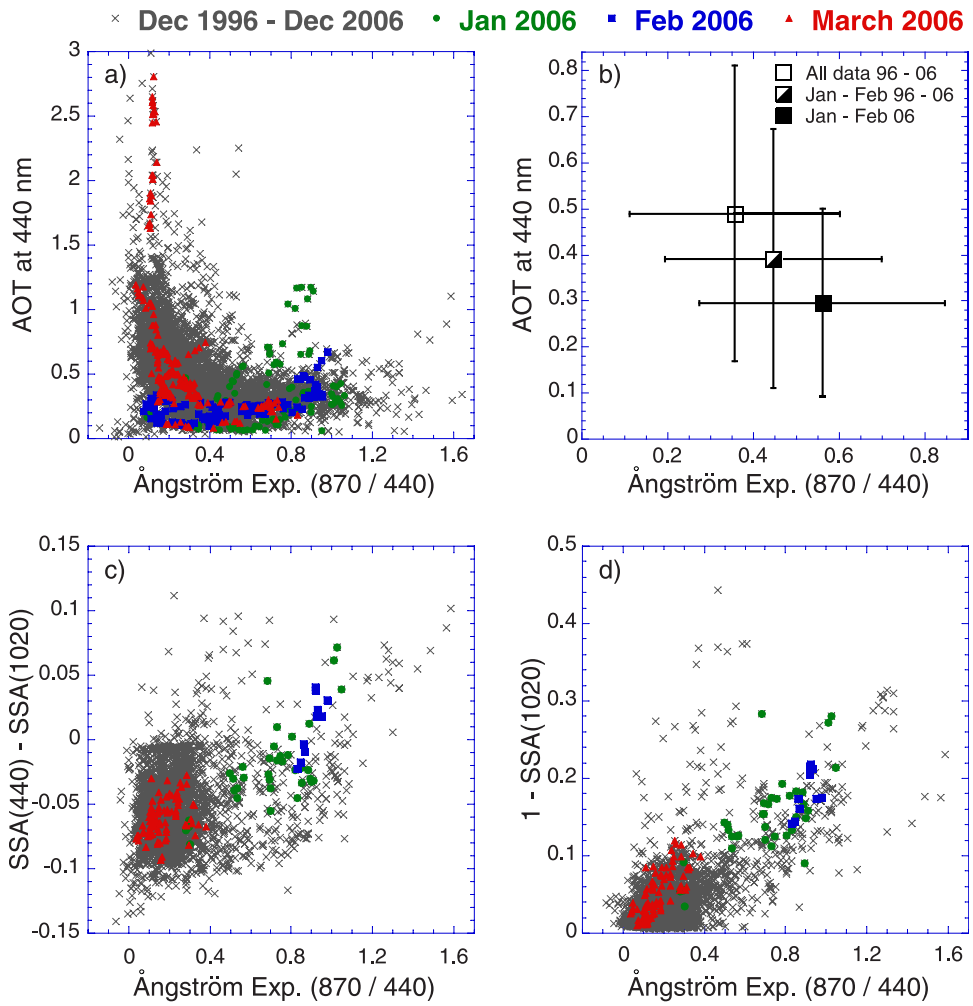

Figure 3. AERONET/PHOTONS observations obtained at the M'Bour site in Senegal. (a) Aerosol optical thickness (AOT) at 440 nm versus Ångström exponent (870/440) for the period of January–March 2006 shown on the background of all the observations from 1996 to 2006. (b) Mean values and associated standard deviations of AOT and Ångström exponent for periods January–February 2006 (SOP-0); January–February from 1996 to 2006; and all the observations from 1996 to 2006. (c) Single scattering albedo (SSA) difference between 440 nm and 1020 nm and (d) 1-SSA (1020 nm) versus Ångström exponent for the period of January–March 2006 shown on the background of all the observations from 1996 to 2006.

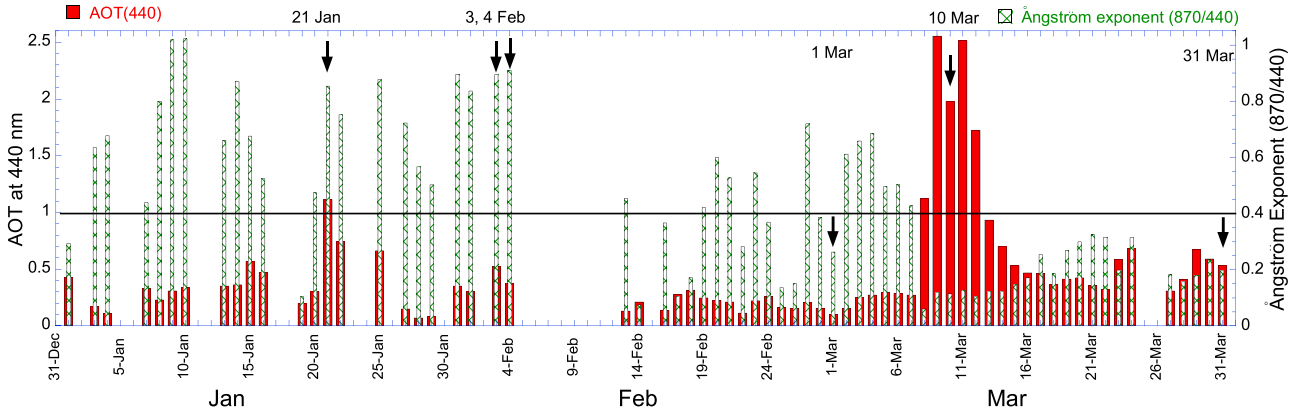

Figure 4. Time series of aerosol optical thickness at 440 nm and Ångström exponent (870/440) for the analyzed period of January–March 2006 with the marked specific events that were selected for a closer analysis.

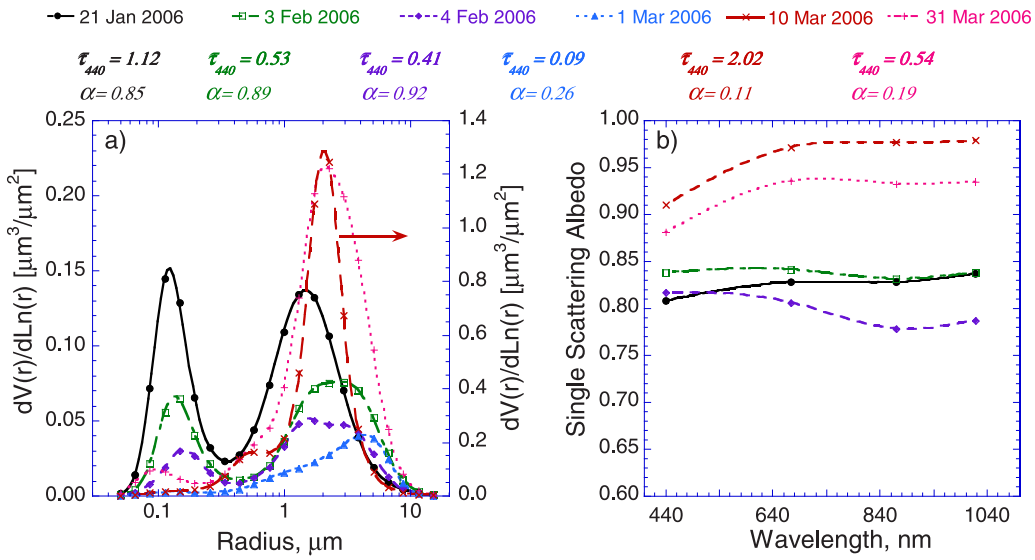

Figure 5. (a) Daily mean aerosol size distributions and (b) spectral single scattering albedo, derived form the AERONET retrievals, for the episodes analyzed. The data is accompanied by corresponded daily mean of aerosol optical thickness at 440 nm and Ångström exponent (870/440). Note that the size distribution for 10 March is related to the right side ordinate.

(α less than about 0.2), but increased absorption for higher contribution of small particles ($0.5 < \alpha < 1.2$) in January–February. As a result, from the scatterplots of $\Delta\omega_0$ and $1 - \omega_0$ versus α in Figures 3c and 3d, we can discriminate the aerosol types by size class and absorbing ability. The data indicate the presence of strongly absorbing at long-wavelengths particles during January and February 2006 with α ranging from 0.5 to 1.2. This intermediate range of α can be attributed to aerosol mixture. Further on, in Figure 5a, we show bimodal aerosol size distributions for observations during January and February 2006 with comparable contributions from both modes, while in March 2006 the coarse mode was dominated.

[16] In summary, although the aerosol loading and dust impact during SOP-0 was below the average, the variability of the possible aerosol sizes and the spectral aerosol absorption features was quite well represented.

4.2. Specific Events Characterization

[17] Many events of increased aerosol burden were observed in the period from January to March 2006. The time series of τ_{ext} and α for this period (Figure 4) shows elevated values of τ_{ext} with significant variability of α. The α value during January–February is relatively high, while a decrease of α is observed on March, which points out the change in the aerosol properties over the region. The time series shows the presence of fine particles during January–February, when the coarse particles governed the aerosol regime in March. We selected several events from this period where successful sun/sky photometer, diffuse and direct radiative flux, and LIDAR measurements were acquired. Additional requirements like the stability of the aerosol load over the day and the absence of clouds leads to the selection of six episodes with range of τ_{ext} from about 0.1 to 2.0 and α from about 0.1 to 0.9.

4.2.1. Aerosol Optical Characteristics

[18] Figure 5 summarizes aerosol size distributions, spectral SSAs, and corresponded τ_{ext} and α of all the selected events. The daily mean τ_{ext} at 440 nm for 21 January and 3 and 4 February was 1.12, 0.53, and 0.41, respectively. On 21 January and 3 and 4 February the atmospheric column aerosol size distributions showed bimodal structure, which typically characterizes aerosol mixture. The ω_0 for these cases was considerably low at all the wavelengths. The SSA for mineral dust usually decreases toward short wavelengths due to the presence of iron oxides. The SSA for anthropogenic pollution aerosols decreases toward long wavelengths [*Dubovik et al.*, 2002] primarily due to absorption by carbonaceous aerosol. However, spectral behavior of ω_0 on 21 January and 3 February was different from typical tendencies for pure mineral dust or pollution. Although the SSA on 21 January showed similarity to dust absorbing feature by slightly lower values at the short wavelengths, the absorption at all the wavelengths is unusually high for mineral dust only. The spectral SSA on 3 February was very low and nearly flat. Despite the fact that the spectral dependence of SSA on 4 February was more similar to the one characterizing pollution aerosol, the SSA values were also very low through the presented spectral range. A possible explanation for the obtained column SSA spectral behavior in January and February can be a combination of dust and biomass burning spectral absorption properties. The column dust absorption could be enhanced by absorbing carbonaceous aerosols and organic compounds existing in biomass burning [e.g., *Andreae and Gelencser*, 2006]. The spectral SSA and bimodal size distribution, as well as α values, which were about 0.85–0.9 for these days, support the hypothesis of the mixed effect of dust and biomass burning aerosols during the selected events.

[19] Significantly different were the size distributions and the spectral SSA for 10 and 31 March. During these events the coarse fraction of the size distribution was clearly

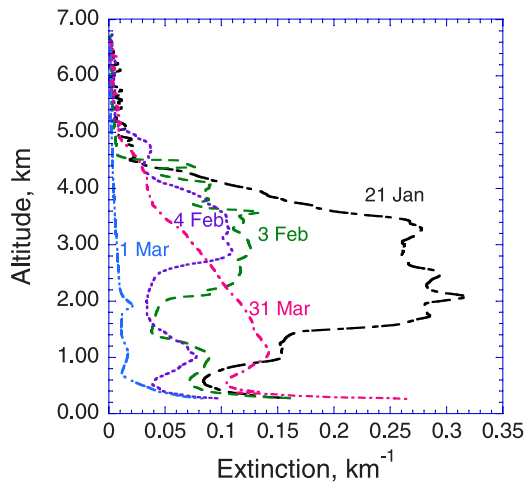

Figure 6. LIDAR derived daily mean aerosol extinction profiles for the analyzed episodes.

dominating and showed a strong dust signal. For 10 and 31 March the daily mean α was 0.11 and 0.19 and the τ_{ext} was 2.02 and 0.54, respectively. The corresponded spectral behavior of SSA for these events fits to the one expected from mineral dust with a stronger short-wavelengths absorption.

[20] On 1 March, aerosol size distribution (Figure 5a) corresponds to a case with very low aerosol loading (τ_{ext} at 440 nm was 0.09). The coarse fraction of the size distribution was dominating and the α of 0.26 indicates dust or probable sea-salt aerosol origin. Low τ_{ext} and dominated coarse fraction are typical for maritime aerosol [*Dubovik et al.*, 2002; *Smirnov et al.*, 2002, 2006]. Indeed, the 5-day air mass backward trajectories, derived with NOAA HYSPLIT Model [*Draxler and Hess*, 1998] (http://www.arl.noaa.gov/ready/hysplit4.html) at the altitudes of 0.5 km and 1 km (not shown), indicated possible aerosol origin in the Atlantic Ocean. However, at the altitude of 3 km the backward trajectory was originated over the Sahel region, circulated over the ocean, and passed over the measurement site. Analysis of the refractive index values showed that this aerosol may not have a pure sea-salt origin. We may have both aerosol types, maritime aerosols in the boundary layer and dust at higher altitudes. The SSA for this case is not presented since an accurate SSA retrieval generally requires higher values of τ_{ext}. This case was employed for illustration of low aerosol loading conditions.

[21] On the basis of the observed size distributions and SSA spectral dependences we can conclude about two possible aerosol types observed from January to March 2006. These are relatively pure mineral dust with presence of iron oxides and mixture of dust and small absorbing particles with carbonaceous compounds, probably of biomass burning origin.

4.2.2. LIDAR Profiles

[22] Vertical profiles of aerosol extinction for the analyzed events were retrieved from LIDAR measurements and reported in Figure 6. The profiles showed two layers or one wide elevated layer structures for the selected events of aerosol mixture. A low-altitude layer was found for the dust event in March. The two layers structure appeared for the mixed aerosol events on 3 and 4 February, where the first layer was from the height of about 0.5 to 1.5 km and the second was from about 2 to 4 km. The extinction profile for the mixed aerosols on 21 January 2006 shows one extended layer located from the height of about 1 km to 4 km. There was no evident aerosol layer for the clearest day on 1 March. Probably a low concentration of sea-salt or dust was maintained in the boundary layer on this day. On 10 March the τ_{ext} was about 2.0 and the LIDAR signal was too strongly attenuated with the altitude, which made the retrieval too difficult. However, for the dust event on 31 March, a maximum of aerosol extinction was observed at about 1 km. This profile suggests one low-altitude layer.

[23] The single wavelength LIDAR cannot provide information on the possible aerosol type at different layers. At the same time, the maximums of the extinction profiles at about 1 km are similar for the cases of the dust event on 31 March and of the aerosol mixture on 3 and 4 February. Assuming that the dust transport conditions are similar in February and March, the second elevated layer in the case of mixture could carry fine aerosol particles of anthropogenic origin. Considering possible enhanced atmospheric convection in fire conditions and consequent aerosol uptake, the aerosols found at the upper layer can be the result of biomass burning rather than of urban or industrial activities. Therefore, these fine aerosols could be transported at high altitudes to Senegal from the Sahel region. The aircraft measurements over the West Africa region in the frame of Dust and Biomass Experiment (DABEX) [*Johnson et al.*, 2008; *Osborne et al.*, 2008] showed the same high-altitude transport of biomass burning aerosol and the low-altitude transport of dust. It was also discussed by *Mallet et al.* [2008] from measurements at the Djougou site in the Northern Benin region. In addition, the 5-day air mass backward trajectories (not shown here), produced with the HYSPLIT model, showed air mass transport at high altitudes (about 3 km) coming from the Sahel region, while at low altitudes (about 0.5 and 1 km) air masses are coming from the Sahara region. Thus, the LIDAR profiles, the aircraft observations, and the air mass backward trajectories confirms that the biomass burning aerosols were transported to the study region at high altitudes during the dry season, while the dust transport occurred at the low altitudes.

4.2.3. Variability in Downward Radiative Fluxes

[24] Atmospheric aerosol loading, scattering properties, and absorption ability are among the factors that control the solar radiation reaching the surface. In this section we analyze the measured diffuse, direct and total downward solar flux and the ratio of direct to total flux for the six selected days (Figure 7). The fluxes are presented as a function of solar zenith angle (SZA).The corresponded daily means of AOT and Ångström exponent are also reported.

[25] A decrease of the direct flux with the increase of aerosol loading and size can be clearly observed in Figure 7a, while the behavior of the diffuse fluxes is opposite (Figure 7b). The variability of the total downward flux (Figure 7c) also depends on the aerosol loading and sizes, although less obvious than for the diffuse or direct flux separately. It has to be noted that an increase of the diffuse flux, and decrease of the direct and the total flux for higher aerosol burden is an expected result. However, Figures 7a, 7b, and 7c provide information about the possible values and diurnal variability

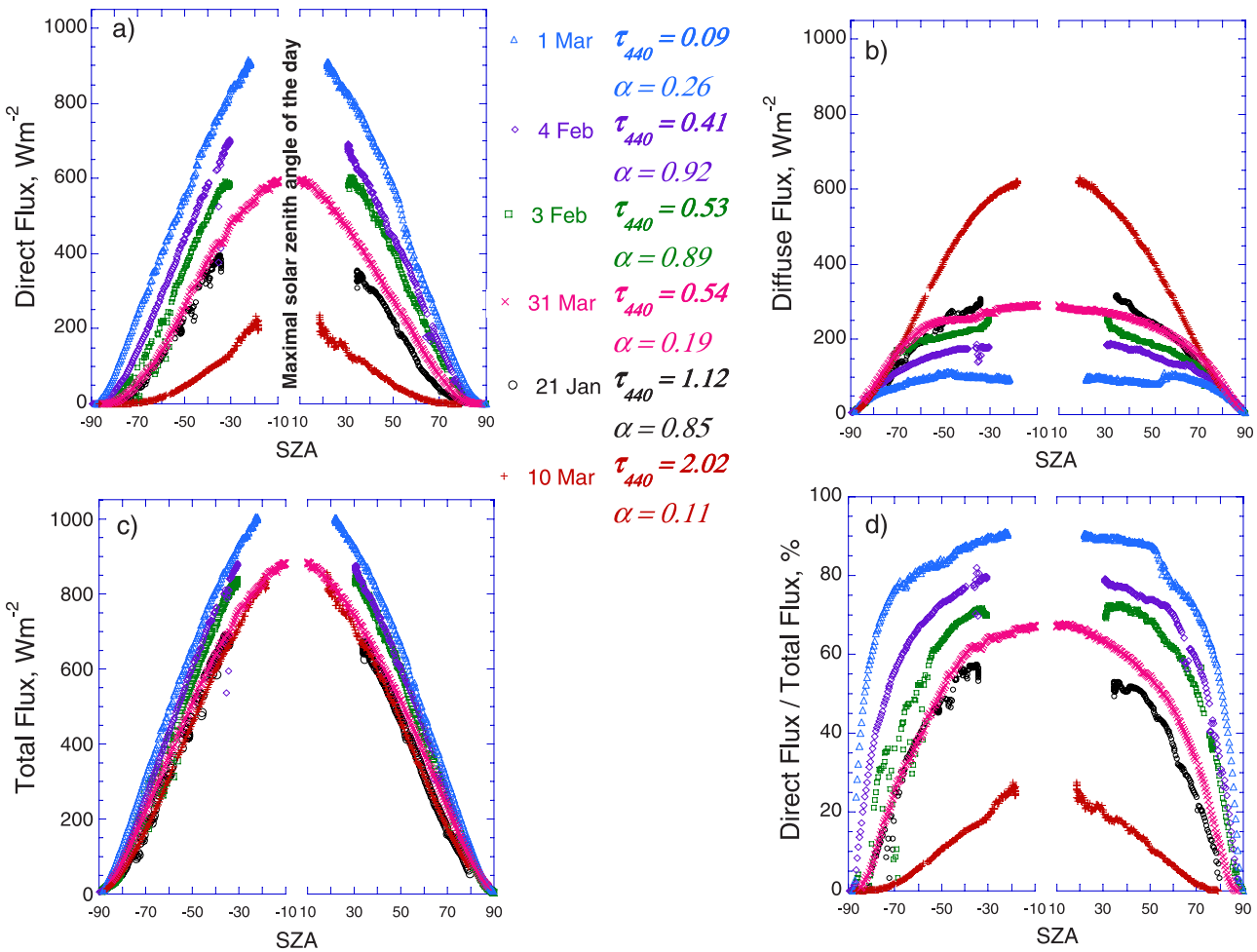

Figure 7. Measured at the surface (a) direct, (b) diffuse, and (c) total downward solar radiative flux and (d) ratio of direct to total flux for all the analyzed events.

of the downward flux corresponding to specific aerosol type and loadings. In addition, in Figure 7d the relative contribution of the direct and diffuse flux to the total shows that the diffuse flux may consist up to 70% of the total flux during noontime and even more for higher solar zenith angles. This observation is important since simulations of scattered light for nonspherical dust particles are complex and may provide uncertainties.

4.2.4. Comparison of the Calculated and Measured Flux

[26] The broadband radiative flux is calculated in the spectral range from 0.2 to 4.0 μm for AERONET observations at the M'Bour site. The operational flux calculations were processed with the atmospheric radiative transfer forward model used in AERONET retrieval code, which considers particles nonsphericity. The detailed retrieved aerosol properties were used for these calculations. The simulation relies on the retrieved complex refractive index at operational wavelengths of CIMEL sun/sky photometer and the retrieved aerosol size distributions. The spectral integration employs real and imaginary parts of refractive index that are interpolated/extrapolated from the values of complex refractive index retrieved at AERONET wavelengths. Spectral dependence of surface reflectance is also interpolated/extrapolated from surface albedo values assumed in the retrieval for the wavelengths of sun/sky photometer. The radiative fluxes are calculated using radiative transfer model GAME (Global Atmospheric Model) [*Dubuisson et al.*, 1996, 2006]. Similar to the operational inversion [*Dubovik and King*, 2000], the flux calculations carefully account for absorption and multiple scattering, as well as their interactions, using Discrete Ordinates code DISORT [see *Stamnes et al.*, 1988; *Nakajima and Tanaka*, 1988]. The GAME model performs spectral integration using correlated k-distribution [*Lacis and Oinas*, 1991] based on line by line simulations for the gaseous absorption [*Dubuisson et al.*, 2004]. More detailed description of the enhanced aerosol properties retrieval from AERONET measurements are currently in preparation by O. Dubovik et al. (manuscript in preparation, 2008).

[27] The relative error between the calculated and the measured values is presented in Figure 8 as a function of τ_{ext} at 440 nm, where the errors of direct, diffuse, and total components are plotted separately. It can be noted that the error in the direct flux increases with τ_{ext}. It shows significantly lower calculated flux compared to the measured one. However, under conditions of heavy aerosol loading, the measured direct flux can be enhanced by strong forward diffuse radiation that can be scattered toward the aperture of the instrument. At the same time, the absolute values of the

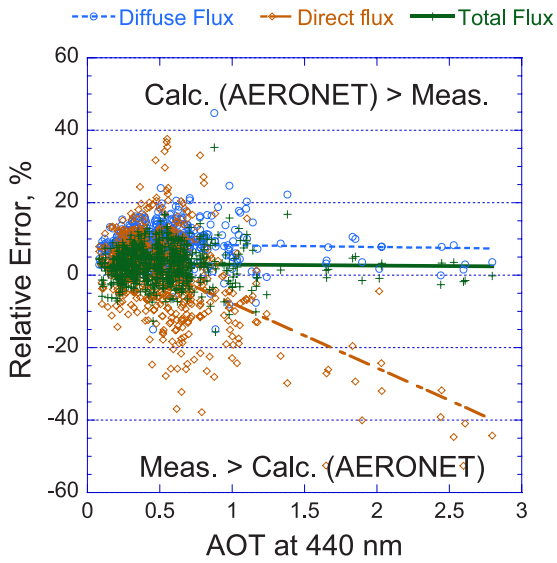

Figure 8. Relative error between the calculated and measured at the surface diffuse, direct and total radiative flux for a range of aerosol optical thicknesses, representing various aerosol loading conditions. Positive values indicate overestimation by calculation.

direct flux are very low for high τ_{ext}. Thus, the increase of the error with the increase of τ_{ext} can be attributed to measurement artifacts rather than to computation errors. The relative error for the diffuse flux showed that computations generally slightly overestimate the measurements. This also results in a slight overestimation of the total flux. The relative error was also analyzed as a function of the solar zenith angle and the Ångström exponent for explanation of possible error sources (figures not shown in this paper), but no evident strong trends of the error were observed. The calculated flux overestimate can result from a too large surface albedo that leads to an overestimate of the downward flux due to additional rereflected component. Indeed, complex surface properties in case of a coastal site increase uncertainty in the assumed angular surface reflectance. This uncertainty, for example, can be verified by simultaneous retrieval of aerosol and surface properties from a combination of AERONET and satellite data [*Sinyuk et al.*, 2007]. Nevertheless, analysis of the relative error between the calculated and measured flux for about 700 coincident observations during 2006 showed that the total calculated flux agrees with the measured within ±10% in 95% of the cases and within ±5% in 73% of the cases. Considering the instrumental uncertainty for our flux

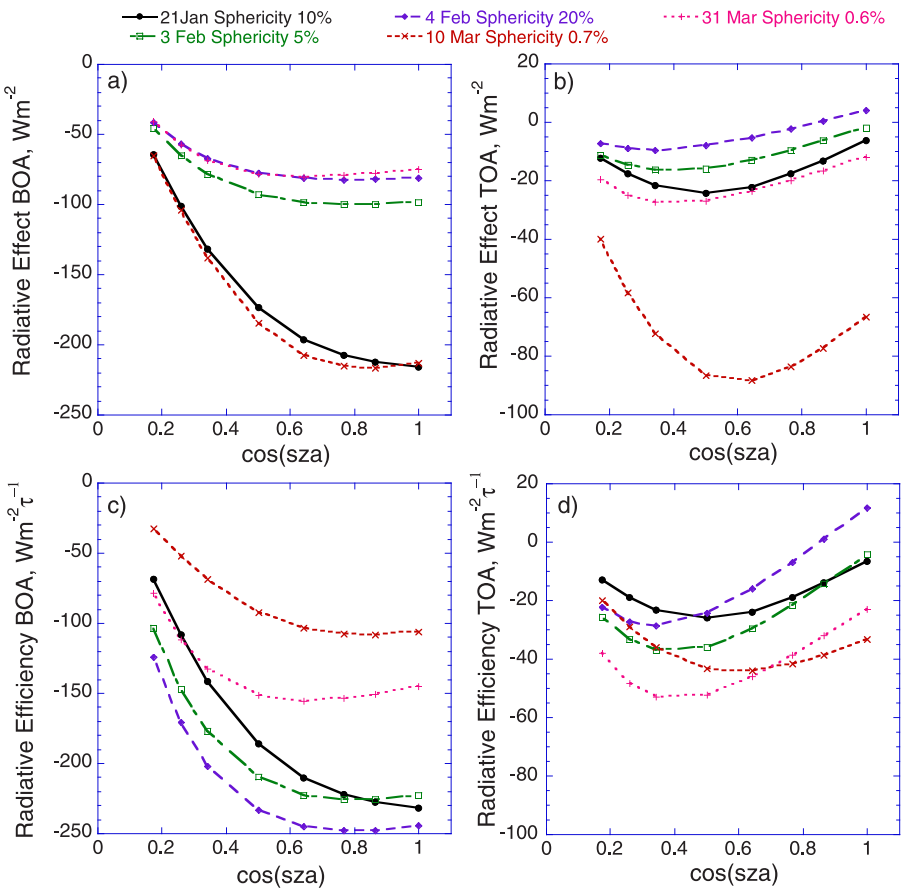

Figure 9. Instantaneous values of aerosol radiative effect at the (a) BOA and (b) TOA and radiative efficiency at the (c) BOA and (d) TOA as a function of cos(SZA). The presented results were calculated by atmospheric radiative transfer forward model employed in AERONET retrieval code. Sphericity percentages, denoted in the legends of the curves, are the aerosol sphericity percentages retrieved by the AERONET inversion algorithm.

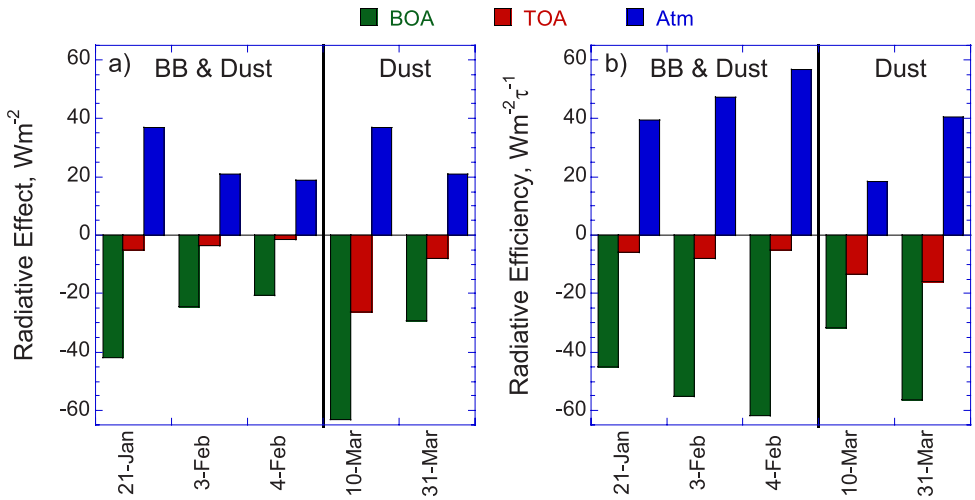

Figure 10. Direct 24-h average aerosol radiative (a) effect and (b) efficiency in cloud-free conditions for the analyzed events of aerosol mixture and predominant mineral dust.

measurements, the agreement between measurements and calculations is quite encouraging.

4.2.5. Aerosol Radiative Effect

[28] In addition to broadband radiative flux, both cloud-free direct aerosol radiative effect (DARE) and radiative efficiency (RE) in short-wavelengths spectral range (0.2–4.0 μm) at the bottom and at the top of the atmosphere (BOA and TOA) are calculated using the AERONET retrieved aerosol properties. Such radiative effect calculations are presently conducted as part of operational processing of AERONET observations (O. Dubovik et al., manuscript in preparation, 2008). The data set was also supplemented by additional radiative effect calculations implemented for a larger number of solar zenith angles (ranging from 0 to 80°). Since successful retrievals of aerosol characteristics require measurements at the large SZAs, the operational calculation of aerosol radiative effect was also conducted in the same conditions. To complete aerosol information for small SZAs, we found that for relatively stable aerosol conditions it is appropriate to use daily averaged values of aerosol size distribution and complex refractive index. We also tested an alternative approach where the aerosol radiative effect determined at the large SZAs was extrapolated toward the smaller SZAs. However, such extrapolation was found less accurate because of variability in the curvature of radiative effect as a function of SZA in different angular ranges.

[29] The aerosol radiative effect at the top and at the bottom of the atmosphere was calculated using the definitions

$$\Delta F_{TOA} = F^0_{TOA} - F_{TOA}$$

$$\Delta F_{BOA} = F_{BOA} - F^0_{BOA},$$

where F^0_{TOA} and F_{TOA} are net (downwelling minus upwelling) fluxes at the TOA in aerosol-free and aerosol-laden atmospheric conditions, respectively; F^0_{BOA} and F_{BOA} are net fluxes at the bottom of the atmosphere for aerosol-free and aerosol-laden conditions, respectively. Thus, negative values of ΔF_{TOA} and ΔF_{BOA} correspond to a cooling effect and positive to warming, either at the TOA or at the BOA [e.g., *Bush and Valero*, 2003; *Roger et al.*, 2006]. The atmospheric aerosol radiative effect was defined as

$$\Delta F_{Atm} = \Delta F_{TOA} - \Delta F_{BOA}.$$

Thus, ΔF_{Atm} introduces part of the remained in the atmosphere radiation and consequently may cause the heating effect. The aerosol radiative efficiency, which is defined as radiative effect per unit aerosol optical thickness, in our study was calculated with respect to τ_{ext} at 550 nm.

[30] Figure 9 represents instantaneous values of aerosol radiative effect and efficiency as a function of cos(SZA). Each curve corresponds to one of the five selected events with aerosol properties reported in Figure 5. The instantaneous aerosol radiative effects at the BOA are presented in Figure 9a. It shows strong surface cooling effect during the event of aerosol mixture on 21 January and during the intensive dust episode on 10 March. It is noteworthy that despite τ_{ext} on 10 March was about two times higher than on 21 January, the radiative effect in both cases was almost similar. It means that at the BOA the radiative efficiency of aerosol mixture can be much higher than of dust alone. The radiative efficiency at the BOA was analyzed and presented in Figure 9c, which confirms enhanced values for the three selected events of aerosol mixture in January–February. However, while at the BOA aerosol mixture produced higher radiative efficiency and cooling effect than dust, at the TOA aerosol mixture led to reduction of negative values (Figures 9b and 9d). This is due to enhanced aerosol absorption of the observed aerosol mixture. Under some conditions the aerosol mixture can cause even positive radiative effect, as it happened, for instance, on 4 February for small SZAs.

[31] The calculated instantaneous values for the range of the solar zenith angles were integrated to derive the 24-h average aerosol radiative effect and efficiency in cloud-free conditions (Figure 10) and summarized in conjunction with the corresponded τ_{ext}, Ångström parameter, fine fraction, SSA, and an average surface reflectance at 657 nm (Table 1). The 24-h average radiative effect and efficiency yielded negative

Table 1. Summary of the Retrieved Aerosol Optical Properties and the Calculated Aerosol Radiative Effect and Efficiency at the M'Bour Site for the Period January–March 2006[a]

	21 January	3 February	4 February	10 March	31 March
Aerosol type	mixture	mixture	mixture	dust	dust
τ_{ext} (440 nm)	1.12	0.53	0.41	2.02	0.54
α(870/440)	0.85	0.89	0.92	0.11	0.19
Fine fraction	0.71	0.73	0.73	0.26	0.33
ω_0 (440 nm)	0.81	0.84	0.82	0.91	0.88
ω_0 (1020 nm)	0.84	0.84	0.79	0.98	0.93
Surf. refl. (657 nm)	0.14	0.15	0.15	0.14	0.16
DARE BOA, Wm^{-2}	−42.0 (1.9%)	−24.5 (2.5%)	−20.5 (3.0%)	−63.3 (7.4%)	−29.1 (8.2%)
DARE TOA, Wm^{-2}	−5.2 (5.5%)	−3.6 (6.0%)	−1.6 (9.5%)	−26.5 (4.6%)	−8.1 (7.6%)
DARE Atm, Wm^{-2}	36.8 (1.4%)	20.9 (1.9%)	18.8 (2.5%)	36.8 (9.4%)	21.0 (8.5%)
RE BOA, $Wm^{-2}\ \tau_{ext}^{-1}$	−45.0 (3.4%)	−55.3 (3.5%)	−61.6 (3.1%)	−31.6 (8.2%)	−56.4 (8.3%)
RE TOA, $Wm^{-2}\ \tau_{ext}^{-1}$	−5.6 (7.1%)	−8.1 (7.1%)	−4.9 (9.6%)	−13.2 (5.3%)	−15.7 (7.7%)
RE Atm, $Wm^{-2}\ \tau_{ext}^{-1}$	39.4 (2.9%)	47.2 (2.9%)	56.7 (2.5%)	18.3 (10.2%)	40.6 (8.5%)

[a]Percentage in parenthesis denotes overestimation of aerosol radiative effect or efficiency due to neglecting particles nonsphericity. DARE is direct aerosol radiative effect in cloud free conditions; RE is aerosol radiative efficiency; BOA is bottom of the atmosphere; TOA is top of the atmosphere; Atm is atmospheric.

values (cooling effect) at the BOA and the TOA for all the events. However, the 24-h average atmospheric radiative effect implied warming of the atmospheric column. It is noteworthy that the BOA and the atmospheric radiative efficiency of the aerosol mixture can be higher than one of the pure dust event, e.g., on 10 March. The daily average radiative efficiency of the mixture at the BOA on 4 February, for example, even exceeds the dust efficiency on 10 March by about 100%. At the TOA radiative efficiency of dust remained dominating compared to aerosol mixture.

4.2.6. Aerosol Nonsphericity in Radiative Effects Simulation

[32] Calculation of broadband radiative flux and estimation of aerosol radiative effect often do not consider differences between spherical and nonspherical particles. It is because the possible angular and spectral differences are expected to be canceled once all contributions of scattered light summed up into the total energy flux. *Mishchenko et al.* [1995] found that the Mie theory can be used for aerosol radiative effect calculations with adequate accuracy even for nonspherical aerosol particles, provided that the aerosol size distribution and AOT are known beforehand. It was noted that since asymmetry parameter is an integrated value, the contrasting nonspherical-spherical differences in the aerosol phase function are averaged out during the integration. The nonspherical-spherical differences in SSA computations were also found as negligible. Therefore, *Mishchenko et al.* [1995] concluded that neglecting small differences in asymmetry parameter caused by particle nonsphericity does not produce significant errors in computations of flux related quantities. Nonetheless, later studies by *Kahnert and Kylling* [2004] and *Kahnert et al.* [2005] based on extensive analysis of asymmetry parameter sensitivity to particle shape concluded that the use of spherical particles model may be among the major error sources in broadband flux simulations.

[33] In the present study we evaluate differences in radiative effect calculations caused by the particle nonsphericity using aerosol optical properties retrieved from AERONET observations for specific desert dust events. It should be noted that radiative computations used here were not limited to using of the integrated value of asymmetry parameter. Instead, 12 moments of phase function expansion were used to account for the details of the aerosol phase function. In addition, the spectral variations of the phase function were included by recalculating phase function at each step of spectral integration from the retrieved size distribution and complex refractive index (interpolated/extrapolated from AERONET retrieved values). The AERONET operational computations relay on nonspherical aerosol phase function for aerosol properties retrieval, as well as for flux calculations. In addition to that computations, we conducted forward flux calculations with the phase function of only spherical particles, while using the exact size distributions and refractive index retrieved with nonspherical model. The values of spectral optical thickness were the same as in operational computations and the shape of the phase function angular dependence was the only factor that could produce a difference in calculated radiative effects compared to operationally produced values. The results showed that neglecting aerosol nonsphericity caused overestimation of aerosol radiative effect at the BOA and the TOA.

[34] Overestimation of instantaneous radiative efficiency at the BOA was higher for dust (up to 9%) than for events of aerosol mixture (up to 4%). At the same time, overestimation of instantaneous radiative efficiency of dust and aerosol mixture at the TOA appeared as similar or even higher for the events of mixture. This is because the TOA radiative efficiency of the mixture yielded small values due to enhanced aerosol absorption. In such condition even minor discrepancy due to the shape assumptions may produce significant relative differences. We also observed that the nonspherical-spherical error dependence on the SZA can change when the aerosol burden is very high (10 March), probably due to the increasing role of multiple scattering that may smooth the nonspherical-spherical differences. The absolute errors in the instantaneous radiative efficiency at the BOA and the TOA as a function of the SZA are shown in Figures 11a and 11b for all the analyzed events.

[35] After averaging the aerosol radiative effect over 24 h, the accounting for particles nonsphericity still appeared significant. The percentage of overestimated 24-h radiative effect and efficiency due to sphericity assumption was summarized in Table 1, along with the calculation results for nonspherical model. For instance, it showed overestimation of aerosol radiative efficiency by about 8% for dust and 3% for mixture at the BOA, and by about 5 or 8% for dust and 7 or 10% for mixture at the TOA. The atmospheric radiative efficiency was overestimated by up to 10% for dust and 3% for mixture. Thus, accounting for aerosol nonsphericity appeared to be important for radiative effects computations of all the events either of dust or mixture.

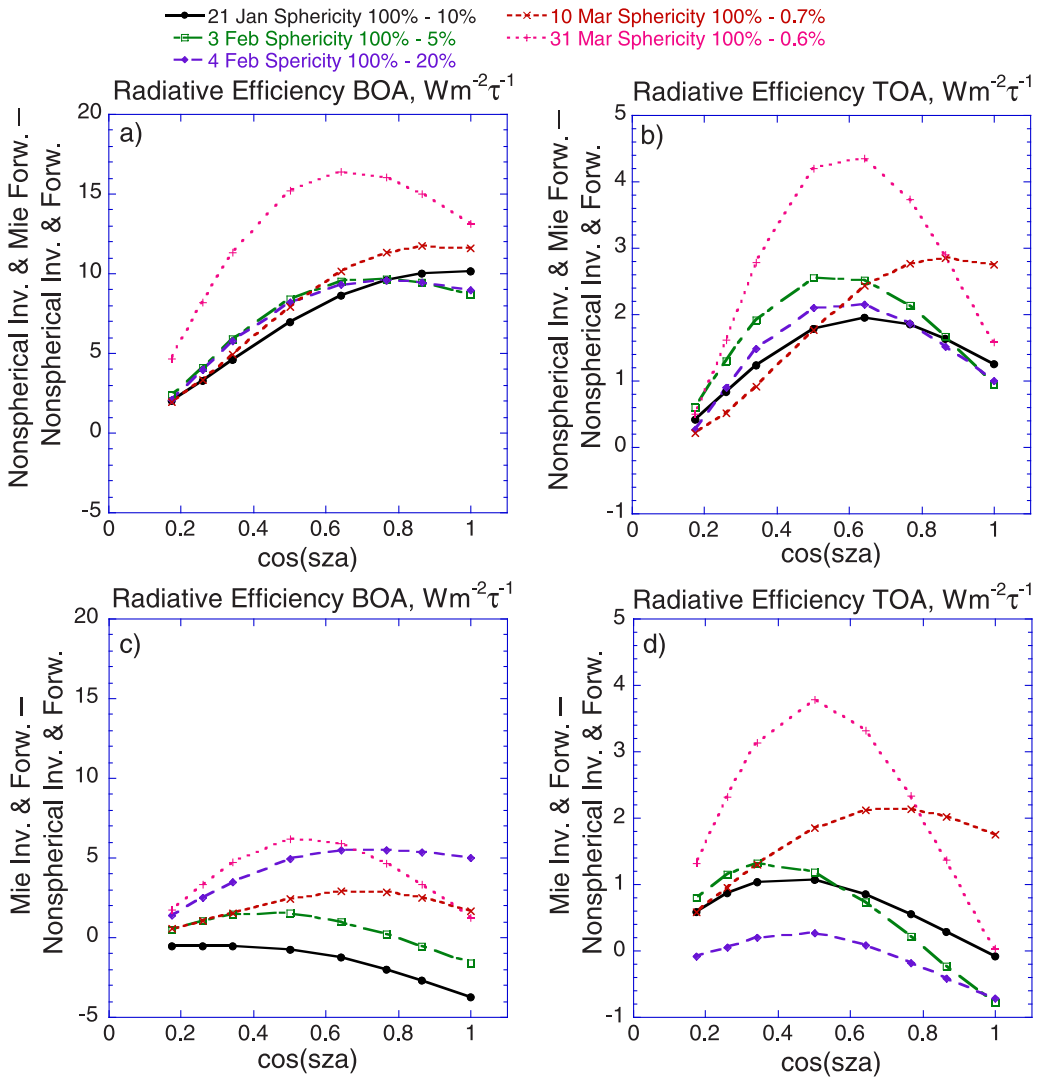

Figure 11. Absolute values of nonspherical-spherical differences for the calculated aerosol radiative efficiencies at the BOA and the TOA as a function of cos(SZA). (a and b) Radiative efficiencies computed for aerosol properties retrieved with nonspherical phase function, but the broadband fluxes were calculated using either the Mie theory or nonspherical phase function. (c and d) Radiative efficiencies computed either with consistent use of the Mie theory or with consistent use of nonspherical phase function. Sphericity percentages denoted in the legends of the curves are either aerosol sphericity percentage retrieved by the AERONET inversion algorithm or the assumed 100% aerosol sphericity. Note that the curves for 21 January and 3 February on Figures 11c and 11d should not be considered as representative.

[36] In this study we also addressed the following question: what is the nonspherical-spherical difference in dust radiative effect computations that could be produced if the Mie theory was consistently used for the retrieval of aerosol properties from Sun photometer observations and then for the broadband flux computations? In order to answer this question we conducted additional calculations where the spherical phase function was used for retrieval of aerosol parameters and also for flux calculations. Then, we compared the obtained aerosol radiative effects with those computed consistently using nonspherical model (operational computations). The analysis showed that the calculated aerosol radiative effects with consistent use of the Mie theory were still higher than those entirely calculated with nonspherical model, although the differences were relatively reduced. The absolute errors in the instantaneous radiative efficiency as a function of the SZA are shown in Figures 11c and 11d. It should be noted here that the inversion with the spheres can produce artifacts in retrieved size distributions or refractive index and it may not fit the measured spectral and angular dependences of observed radiation [*Dubovik et al.*, 2006]. For example, the retrieved aerosol models for several observations on 21 January and 3 February were found as unreliable when using spherical assumption in the inversion procedure. For this reason the nonspherical-spherical differences for these days in Figures 11c and 11d should not be considered as representative. However, for the other cases the nonspherical-spherical differences in the calculated

aerosol radiative efficiency were clearly due to the distinction in the phase function only. Summarizing this analysis we would like to note that in aerosol radiative effects computations the aerosol properties (size distribution and refractive index) are often known beforehand. In such situation using nonspherical phase function seems to provide more realistic properties for desert dust aerosol. In this context the observed overestimation of dust or aerosol mixture radiative effects presented in Table 1 and Figures 11a and 11b should be considered as more relevant. Therefore, once the Mie theory is employed for broadband flux calculations, the systematic overestimation may appear in dust radiative effects and efficiencies computations. For example, it may occur in computations relying on aerosol size distributions and refractive indices obtained from direct measurements or produced by chemical transport models.

5. Summary and Conclusions

[37] The atmospheric aerosol optical properties and aerosol radiative effects on climate were studied at the M'Bour site, Senegal. The work was conducted in the frame of the African Monsoon Multidisciplinary Analysis (AMMA) program. We focused on the period of the dry phase of the monsoon cycle when the study area is affected by airborne mineral dust and biomass burning aerosol particles. Several episodes with aerosol mixture and predominant mineral dust conditions were analyzed and presented in the context of previous years' observations. The aerosol size and spectral absorption characteristics, in conjunction with the measured vertical profiles and transport features, indicated that the aerosol mixture was composed from mineral dust and biomass burning aerosols. The presence of biomass burning aerosols was also consistent with other parallel studies in the region [*Johnson et al.*, 2008; *Osborne et al.*, 2008].

[38] It was found that during the special observing period (SOP-0) the aerosol loading was 25% below the average for the same period of previous years. Analysis of AOT from MODIS space instrument also showed considerably lower aerosol loading over the Western Africa region in January–February 2006. As a result, the aerosol climatic impact during the dry season in 2006 can differ from the previous years, but aerosol sizes and spectral absorption features are quite representative of the M'Bour site.

[39] The vertical profiles of the aerosol extinction, derived from LIDAR measurements during the aerosol mixture events, showed two layers and one wide elevated layer structures. Analysis of the obtained profiles suggested high-altitude transport (up to about 4 km) of biomass burning aerosol. The evidence of high-altitude biomass burning aerosol transport was also found during aircraft observations in the region [*Johnson et al.*, 2008; *Osborne et al.*, 2008]. The mineral dust transport apparently was at the lower altitudes of about 0.5 to 1.5 km in the period from January to March 2006, a pattern which is also consistent with previous observations of low dust transport layers in the winter months [*Chiapello et al.*, 1995]. The retrieved aerosol size distributions from AERONET showed bimodality with significant fine and coarse fractions for the events with the elevated aerosol layers. The retrieved spectral single scattering albedo was very low, indicating highly absorbing aerosols at all the wavelengths from 440 nm to 1020 nm that could have an impact on atmospheric convection dynamics.

[40] The broadband downward radiative flux was continuously measured at the M'Bour site during the observation period. We have presented diurnal variability of radiative flux for events where AOT at 440 nm ranged from 0.1 to 2.0 and the Ångström exponent ranged from 0.1 to 0.9. The diffuse and direct radiative flux at the surface showed evident dependence on aerosol concentrations and type. The analysis illustrated the possible values of the downward flux in various aerosol conditions. In addition, the observed dominated diffuse radiation, during the dust events, emphasized the importance of accurate diffuse radiation simulation for nonspherical particles. The calculated broadband radiative flux showed general agreement with the measurements within ±10% or better.

[41] The aerosol radiative effect and efficiency were then calculated with the detailed retrieved aerosol characteristics using the AERONET code. The radiative efficiency of mixed biomass burning aerosol with mineral dust appeared as different from the one of pure mineral dust. It was found that in some cases such mixture can block the solar radiation reaching the surface almost twice more efficiently than dust only. The apparent reason for this effect is an enhanced absorption ability of the mixture. For example, a strong pure dust event on 10 March 2006 produced the aerosol radiative efficiency at the BOA of -31.6 Wm^{-2} τ_{ext}^{-1}, while the events of aerosol mixture yielded higher values of -45.0 to -61.6 Wm^{-2} τ_{ext}^{-1}. The obtained aerosol radiative efficiency at the BOA was in agreement with the parallel study presented by *Mallet et al.* [2008] for a region affected by biomass burning aerosol. However, the values at the TOA could be different probably due to a variety in the surface properties. The TOA radiative effect and efficiency for all the analyzed events were negative and indicated cooling of the surface. The radiative effect and efficiency of dust at the TOA were stronger than of highly absorbing aerosol mixture. The TOA radiative efficiency of dust was -13.2 to -15.7 Wm^{-2} τ_{ext}^{-1}, while the mixture yielded values of -4.9 to -8.1 Wm^{-2} τ_{ext}^{-1}.

[42] In addition, for the analyzed aerosol episodes we tested the impact of neglecting aerosol nonsphericity on radiative effect calculations. Our results showed that assumption on particles sphericity in aerosol radiative effect calculations lead to an overestimation of the aerosol cooling effect. The 24-h average direct aerosol radiative effect can be biased; in the analyzed cases it was overestimated by about 2 to 8% at the BOA and about 5 to 10% at the TOA due to neglecting the nonspherical shape of aerosol particles.

[43] **Acknowledgments.** On the basis of a French initiative, AMMA was built by an international scientific group and is currently funded by a large number of agencies, especially from France, UK, United States, and Africa. It has been the beneficiary of a major financial contribution from the European Community's Sixth Framework Research Programme. Detailed information on scientific coordination and funding is available on the AMMA International Web site http://www.amma-international.org. The authors thank all members of the AERONET group, led by Brent N. Holben, for data processing. Also the authors thank all members of PHOTONS group, which is the French part of AERONET led by Philippe Goloub, for operation of the M'Bour (Dakar) site. In addition, the authors are very thankful to Bernadette Chatenet of the Laboratoire Interuniversitaire des Systémes Atmosphériques for managing the M'Bour long-term site. Also we thank Tamsir Diop, Aboubacri Dialo, and the staff of the Institut de Recherche et Développement responsible for maintaining the

instruments in properly working conditions and for their great contribution to the data quality. Analyses and visualizations of the MODIS product used in this paper were produced with the Giovanni online data system, developed and maintained by the NASA Goddard Earth Sciences (GES) Data and Information Services Center (DISC). We also acknowledge the MODIS mission scientists and associated NASA personnel for the production of the data used in this research effort. The authors gratefully acknowledge the NOAA Air Resources Laboratory (ARL) for the provision of the HYSPLIT transport and dispersion model and the READY Web site (http://www.arl.noaa.gov/ready.html) used in this publication.

References

Andreae, M. O., and A. Gelencser (2006), Black carbon or brown carbon? The nature of light-absorbing carbonaceous aerosols, *Atmos. Chem. Phys.*, *6*, 3131–3148.

Bush, B. C., and F. P. J. Valero (2003), Surface aerosol radiative forcing at Gosan during the ACE-Asia campaign, *J. Geophys. Res.*, *108*(D23), 8660, doi:10.1029/2002JD003233.

Chiapello, I., G. Bergametti, L. Gomes, B. Chatenet, F. Dulac, J. Pimenta, and E. S. Suares (1995), An additional low layer transport of Sahelian and Saharan dust over the north-eastern tropical Atlantic, *Geophys. Res. Lett.*, *22*(23), 3191–3194, doi:10.1029/95GL03313.

Chiapello, I., G. Bergametti, B. Chatenet, P. Bousquet, F. Dulac, and E. S. Soares (1997), Origins of African dust transported over the northeastern tropical Atlantic, *J. Geophys. Res.*, *102*(D12), 13,701–13,709, doi:10.1029/97JD00259.

Draxler, R. R., and G. D. Hess (1998), An overview of the Hysplit_4 modeling system for trajectories, *Aust. Meteorol. Mag.*, *47*, 295–308.

Dubovik, O., and M. D. King (2000), A flexible inversion algorithm for retrieval of aerosol optical properties from Sun and sky radiance measurements, *J. Geophys. Res.*, *105*(D16), 20,673–20,696, doi:10.1029/2000JD900282.

Dubovik, O., B. Holben, T. F. Eck, A. Smirnov, Y. J. Kaufman, M. D. King, D. Tanre, and I. Slutsker (2002), Variability of absorption and optical properties of key aerosol types observed in worldwide locations, *J. Atmos. Sci.*, *59*(3), 590–608, doi:10.1175/1520-0469(2002)059<0590:VOAAOP>2.0.CO;2.

Dubovik, O., et al. (2006), Application of spheroid models to account for aerosol particle nonsphericity in remote sensing of desert dust, *J. Geophys. Res.*, *111*, D11208, doi:10.1029/2005JD006619.

Dubuisson, P., J. C. Buriez, and Y. Fouquart (1996), High spectral resolution solar radiative transfer in absorbing and scattering media: Application to the satellite simulation, *J. Quant. Spectrosc. Radiat. Transfer*, *55*(1), 103–126, doi:10.1016/0022-4073(95)00134-4.

Dubuisson, P., D. Dessailly, M. Vesperini, and R. Frouin (2004), Water vapor retrieval over ocean using near-infrared radiometry, *J. Geophys. Res.*, *109*, D19106, doi:10.1029/2004JD004516.

Dubuisson, P., J. C. Roger, M. Mallet, and O. Dubovik (2006), A code to compute the direct solar radiative forcing: Application to anthropogenic aerosols during the Escompte experiment, in *IRS 2004: Current Problems in Atmospheric Radiation*, edited by H. Fischer and B.-J. Sohn, pp. 127–130, A. Deepak, Hampton, Va.

Eck, T. F., et al. (2003), Variability of biomass burning aerosol optical characteristics in southern Africa during the SAFARI 2000 dry season campaign and a comparison of single scattering albedo estimates from radiometric measurements, *J. Geophys. Res.*, *108*(D13), 8477, doi:10.1029/2002JD002321.

Formenti, P., W. Elbert, W. Maenhaut, J. Haywood, and M. O. Andreae (2003), Chemical composition of mineral dust aerosol during the Saharan Dust Experiment (SHADE) airborne campaign in the Cape Verde region, September 2000, *J. Geophys. Res.*, *108*(D18), 8576, doi:10.1029/2002JD002648.

Haywood, J., P. Francis, S. Osborne, M. Glew, N. Loeb, E. Highwood, D. Tanre, G. Myhre, P. Formenti, and E. Hirst (2003), Radiative properties and direct radiative effect of Saharan dust measured by the C-130 aircraft during SHADE: 1. Solar spectrum, *J. Geophys. Res.*, *108*(D18), 8578, doi:10.1029/2002JD002552.

Highwood, E. J., J. M. Haywood, M. D. Silverstone, S. M. Newman, and J. P. Taylor (2003), Radiative properties and direct effect of Saharan dust measured by the C-130 aircraft during Saharan Dust Experiment (SHADE): 2. Terrestrial spectrum, *J. Geophys. Res.*, *108*(D18), 8578, doi:10.1029/2002JD002552.

Holben, B. N., T. F. Eck, I. Slutsker, D. Tanre, J. P. Buis, A. Setzer, E. Vermote, J. A. Reagan, Y. J. Kaufman, and T. Nakajima (1998), AERONET-A federated instrument network and data archive for aerosol characterization, *Remote Sens. Environ.*, *66*(1), 1–16, doi:10.1016/S0034-4257(98)00031-5.

Holben, B. N., et al. (2001), An emerging ground-based aerosol climatology: Aerosol optical depth from AERONET, *J. Geophys. Res.*, *106*(D11), 12,067–12,097, doi:10.1029/2001JD900014.

Ichoku, C., L. A. Remer, Y. J. Kaufman, R. Levy, D. A. Chu, D. Tanre, and B. N. Holben (2003), MODIS observation of aerosols and estimation of aerosol radiative forcing over southern Africa during SAFARI 2000, *J. Geophys. Res.*, *108*(D13), 8499, doi:10.1029/2002JD002366.

Johnson, B. T., S. R. Osborne, and J. M. Haywood (2008), Aircraft measurements of biomass-burning aerosols over West Africa during DABEX, *J. Geophys. Res.*, *113*, D00C06, doi:10.1029/2007JD009451.

Kahnert, M., and A. Kylling (2004), Radiance and flux simulations for mineral dust aerosols: Assessing the error due to using spherical or spheroidal model particles, *J. Geophys. Res.*, *109*, D09203, doi:10.1029/2003JD004318.

Kahnert, M., T. Nousiainen, and B. Veihelmann (2005), Spherical and spheroidal model particles as an error source in aerosol climate forcing and radiance computations: A case study for feldspar aerosols, *J. Geophys. Res.*, *110*, D18S13, doi:10.1029/2004JD005558.

Kaufman, Y. J., D. Tanré, L. A. Remer, E. F. Vermote, A. Chu, and B. N. Holben (1997), Operational remote sensing of tropospheric aerosol over land from EOS moderate resolution imaging spectroradiometer, *J. Geophys. Res.*, *102*(D14), 17,051–17,067, doi:10.1029/96JD03988.

Kaufman, Y. J., I. Koren, L. A. Remer, D. Tanre, P. Ginoux, and S. Fan (2005), Dust transport and deposition observed from the Terra-Moderate Resolution Imaging Spectroradiometer (MODIS) spacecraft over the Atlantic Ocean, *J. Geophys. Res.*, *110*, D10S12, doi:10.1029/2003JD004436.

Kirchstetter, T. W., T. Novakov, and P. V. Hobbs (2004), Evidence that the spectral dependence of light absorption by aerosols is affected by organic carbon, *J. Geophys. Res.*, *109*, D21208, doi:10.1029/2004JD004999.

Klett, J. D. (1981), Stable analytical inversion solution for processing lidar returns, *Appl. Opt.*, *20*(2), 211–220.

Lacis, A. A., and V. Oinas (1991), A description of the correlated kappa-distribution method for modeling nongray gaseous absorption, thermal emission, and multiple-scattering in vertically inhomogeneous atmospheres, *J. Geophys. Res.*, *96*(D5), 9027–9063, doi:10.1029/90JD01945.

Liousse, C., J. E. Penner, C. Chuang, J. J. Walton, H. Eddleman, and H. Cachier (1996), A global three-dimensional model study of carbonaceous aerosols, *J. Geophys. Res.*, *101*(D14), 19,411–19,432, doi:10.1029/95JD03426.

Mallet, M., et al. (2008), Aerosol direct radiative forcing on Djougou (northern Benin) during the African Monsoon Multidisciplinary Analysis dry season experiment (Special Observation Period-0), *J. Geophys. Res.*, *113*, D00C01, doi:10.1029/2007JD009419.

Mishchenko, M. I., A. A. Lacis, B. E. Carlson, and L. D. Travis (1995), Nonsphericity of dust-like tropospheric aerosols: Implications for aerosol remote sensing and climate modeling, *Geophys. Res. Lett.*, *22*(9), 1077–1080, doi:10.1029/95GL00798.

Mishchenko, M. I., L. D. Travis, R. A. Kahn, and R. A. West (1997), Modeling phase functions for dustlike tropospheric aerosols using a shape mixture of randomly oriented polydisperse spheroids, *J. Geophys. Res.*, *102*(D14), 16,831–16,847, doi:10.1029/96JD02110.

Myhre, G., A. Grini, J. M. Haywood, F. Stordal, B. Chatenet, D. Tanre, J. K. Sundet, and I. S. A. Isaksen (2003), Modeling the radiative impact of mineral dust during the Saharan Dust Experiment (SHADE) campaign, *J. Geophys. Res.*, *108*(D18), 8579, doi:10.1029/2002JD002566.

Nakajima, T., and M. Tanaka (1988), Algorithms for radiative intensity calculations in moderately thick atmospheres using a truncation approximation, *J. Quant. Spectrosc. Radiat. Transfer*, *40*(1), 51–69, doi:10.1016/0022-4073(88)90031-3.

Osborne, S. R., B. T. Johnson, and J. M. Haywood (2008), Physical and optical properties of mineral dust aerosol during the Dust and Biomass Experiment (DABEX), *J. Geophys. Res.*, *113*, D00C03, doi:10.1029/2007JD009551.

Privette, J. L., and D. P. Roy (2005), Southern Africa as a remote sensing test bed: The SAFARI 2000 special issue overview, *Int. J. Remote Sens.*, *26*(19), 4141–4158, doi:10.1080/01431160500113401.

Ramanathan, V., et al. (2001), Indian Ocean Experiment: An integrated analysis of the climate forcing and effects of the great Indo-Asian haze, *J. Geophys. Res.*, *106*(D22), 28,371–28,398, doi:10.1029/2001JD900133.

Remer, L. A., et al. (2005), The MODIS aerosol algorithm, products, and validation, *J. Atmos. Sci.*, *62*(4), 947–973, doi:10.1175/JAS3385.1.

Roger, J. C., M. Mallet, P. Dubuisson, H. Cachier, E. Vermote, O. Dubovik, and S. Despiau (2006), A synergetic approach for estimating the local direct aerosol forcing: Application to an urban zone during the Experience sur Site pour Contraindre les Modeles de Pollution et de Transport d'Emission (ESCOMPTE) experiment, *J. Geophys. Res.*, *111*(13), D13208, doi:10.1029/2005JD006361.

Sinyuk, A., et al. (2007), Simultaneous retrieval of aerosol and surface properties from a combination of AERONET and satellite data, *Remote Sens. Environ.*, *107*(1–2), 90–108, doi:10.1016/j.rse.2006.07.022.

Smirnov, A., B. N. Holben, T. F. Eck, O. Dubovik, and I. Slutsker (2000), Cloud-screening and quality control algorithms for the AERONET data-

base, *Remote Sens. Environ.*, *73*(3), 337–349, doi:10.1016/S0034-4257(00)00109-7.

Smirnov, A., B. N. Holben, Y. J. Kaufman, O. Dubovik, T. F. Eck, I. Slutsker, C. Pietras, and R. N. Halthore (2002), Optical properties of atmospheric aerosol in maritime environments, *J. Atmos. Sci.*, *59*(3), 501–523, doi:10.1175/1520-0469(2002)059<0501:OPOAAI>2.0.CO;2.

Smirnov, A., et al. (2006), Ship-based aerosol optical depth measurements in the Atlantic Ocean: Comparison with satellite retrievals and GOCART model, *Geophys. Res. Lett.*, *33*, L14817, doi:10.1029/2006GL026051.

Sokolik, I. N., and O. B. Toon (1999), Incorporation of mineralogical composition into models of the radiative properties of mineral aerosol from UV to IR wavelengths, *J. Geophys. Res.*, *104*(D8), 9423–9444, doi:10.1029/1998JD200048.

Stamnes, K., S. C. Tsay, W. Wiscombe, and K. Jayaweera (1988), Numerically stable algorithm for discrete-ordinate-method radiative-transfer in multiple-scattering and emitting layered media, *Appl. Opt.*, *27*(12), 2502–2509.

Swap, R. J., et al. (2002), The Southern African Regional Science Initiative (SAFARI 2000), Overview of the dry season field campaign, *S. Afr. J. Sci.*, *98*(3–4), 125–130.

Tanré, D., Y. J. Kaufman, M. Herman, and S. Mattoo (1997), Remote sensing of aerosol properties over oceans using the MODIS/EOS spectral radiances, *J. Geophys. Res.*, *102*(D14), 16,971–16,988, doi:10.1029/96JD03437.

Tanré, D., J. Haywood, J. Pelon, J.-F. Léon, B. Chatenet, P. Formenti, P. Francis, P. Goloub, E. J. Highwood, and G. Myhre (2003), Measurement and modeling of the Saharan dust radiative impact: Overview of the Saharan Dust Experiment (SHADE), *J. Geophys. Res.*, *108*(D18), 8574, doi:10.1029/2002JD003273.

Volten, H., O. Munoz, E. Rol, J. F. de Haan, W. Vassen, J. W. Hovenier, K. Muinonen, and T. Nousiainen (2001), Scattering matrices of mineral aerosol particles at 441.6 nm and 632.8 nm, *J. Geophys. Res.*, *106*(D15), 17,375–17,401, doi:10.1029/2001JD900068.

F. Auriol, G. Brogniez, I. Chiapello, Y. Derimian, O. Dubovik, J.-F. Léon, T. Podvin, and D. Tanré, Laboratoire d'Optique Atmosphérique, Université des Sciences et Technologies de Lille, CNRS, F-59655 Villeneuve d'Ascq, France. (derimian@loa.univ-lille1.fr)

B. N. Holben and A. Sinyuk, Laboratory for Terrestrial Physics, NASA Goddard Space Flight Center, Greenbelt, MD 20771, USA.